Int. J. Heat Mass Transfer. Vol. 33, No. 2, pp. 367–380, 1990
Printed in Great Britain

0017–9310/90 $3.00 + 0.00

Numerical simulation of solidification in a horizontal cylindrical annulus charged with an aqueous salt solution

D. G. NEILSON and F. P. INCROPERA
Heat Transfer Laboratory, School of Mechanical Engineering, Purdue University, West Lafayette, IN 47907, U.S.A.

and

W. D. BENNON
Alcoa Technical Center, Alcoa Center, PA 15069, U.S.A.

(*Received* 27 *December* 1988 *and in final form* 2 *June* 1989)

Abstract—A computational study of solidification of a binary Na_2CO_3 solution in a horizontal cylindrical annulus is performed using a continuum formulation with a control-volume based, finite-difference scheme. The initial conditions were selected to facilitate the study of counter thermal and solutal convection, accompanied by extensive mushy region growth. Numerical results are compared with experimental data with mixed success. Qualitative agreement is obtained for the overall solidification process and associated physical phenomena. However, the plume thickness calculated for the solutally-driven convective upflow is substantially smaller than the observed value. Evolution of double-diffusive layers is predicted, but over a time scale much smaller than that observed experimentally. Good agreement is obtained between predicted and measured results for solid growth, but the mushy region thickness is significantly overpredicted.

1. INTRODUCTION

A UNIQUE feature of solidification of non-eutectic, binary solutions is the coexistence of solid and liquid phases over an extended temperature range. Phase transition from liquid to solid is further characterized by selective component rejection, which promotes the development of compositional gradients in the two-phase (mushy) and neighboring pure liquid regions. Natural convection induced by these solutal gradients, as well as by thermal gradients, has a pronounced influence on the solidification process. In a metallurgical context, such flows have been identified as mechanisms responsible for localized remelting and segregate formation (macrosegregation) during the casting of alloys [1]. Other systems or processes that involve multicomponent phase change are associated with latent energy storage [2], crystal growth [3], and life sciences [4].

Due to recent interest in binary solution solidification, several investigators have developed generalized theoretical models to predict transport phenomena during the phase change process. Comparisons of model predictions with the results of experiments performed using metal alloy analogs in simplified geometries have been encouraging. Thompson and Szekely [5] developed a two-domain solidification model that assumed the mushy region to be of negligible thickness but included thermal and solutal natural convection in the liquid. The transient response of an aqueous salt solution (Na_2CO_3) crystallized from a vertical wall in a rectangular cavity was predicted, and favorable agreement was obtained with experimental results, particularly with respect to the existence of double-diffusive convection effects, non-planar growth, and the magnitude of convective velocities.

Continuum theory was utilized by Bennon and Incropera [6] to develop a mathematical model capable of predicting solid, mushy, and liquid phase transport phenomena. Use of an enthalpy-based energy conservation equation [7] eliminated the need to specify interface boundary conditions at the solidus and liquidus fronts. Computations were performed for freezing along a vertical wall in a two-dimensional rectangular cavity [8], and the ability to predict thermal and solutal flows in the mushy region, segregate formation, and remelting was demonstrated. Comparisons between experimental and predicted results for the rectangular cavity [9, 10] agree with respect to important qualitative features, such as the nature of the flows and solute redistribution, but fail to achieve close quantitative agreement.

Although the aforementioned studies have addressed phase change phenomena for the two-dimensional rectangular cavity, the horizontal annular cavity also represents an important engineering geometry, particularly for energy storage devices and metal castings. To date, no computations have been reported which investigate the solidification of a binary solution in an annulus with freezing from the inner cylinder. Accordingly, it is the objective of this

NOMENCLATURE

c	specific heat
B	buoyancy force per unit volume
D	mass diffusion coefficient or cylinder diameter
f	mass fraction (local)
$\bar{f}$	mass fraction (overall)
f^*	dimensionless liquid composition
g	volume fraction or gravitational acceleration
h	enthalpy
k	thermal conductivity
p	pressure
$\bar{q}$	average heat extraction rate
t	time or thickness
T	temperature
u, v	θ-, r-direction velocity components
$\mathbf{v}$	velocity vector
θ, r	polar coordinates.

Greek symbols

β_s	solutal expansion coefficient
β_T	thermal expansion coefficient
θ^*	dimensionless temperature
κ	permeability
μ	dynamic viscosity
ρ	density
ψ	streamfunction.

Subscripts

c	cylinder
e	eutectic
i	inner
l	liquid
m	mushy
o	initial or outer
S	solutal
s	solid or surface
T	thermal.

Superscript

α	Na_2CO_3.

work to numerically simulate this solidification process and to compare model predictions with experimental results.

2. MATHEMATICAL MODEL

The continuum formulation for modelling binary solidification [6] has been adopted in the present study. For a two-dimensional (r, θ) cylindrical geometry (Fig. 1), the continuum conservation equations for mass, θ-momentum, r-momentum, energy and species may be expressed, respectively, as

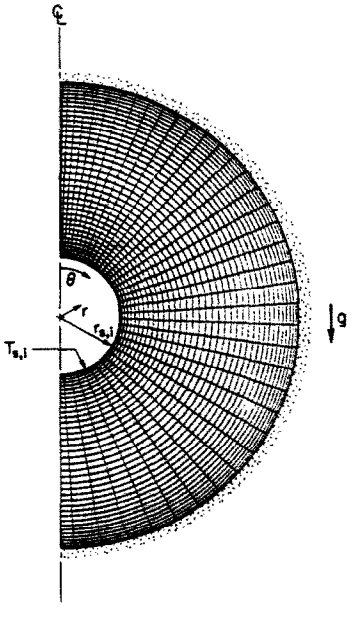

FIG. 1. Schematic of the physical system and computational domain.

$$\frac{\partial \rho}{\partial t} + \nabla \cdot (\rho \mathbf{v}) = 0 \tag{1}$$

$$\frac{\partial(\rho u)}{\partial t} + \nabla \cdot (\rho \mathbf{v} u) = \nabla \cdot \left(\mu_l \frac{\rho}{\rho_l} \nabla u \right) - \frac{1}{r} \frac{\partial p}{\partial \theta} + B_\theta - \frac{\mu_l}{\kappa} \frac{\rho}{\rho_l} (u - u_s) + \frac{2}{r} \mu_l \frac{\partial}{\partial \theta} \left(\frac{\rho}{\rho_l} (v - f_s v_s) \right) - \frac{1}{r^2} \mu_l \frac{\rho}{\rho_l} (u - f_s u_s) - \rho \left(f_s \frac{u_s v_s}{r} + f_l \frac{u_l v_l}{r} \right) \tag{2}$$

$$\frac{\partial(\rho v)}{\partial t} + \nabla \cdot (\rho \mathbf{v} v) = \nabla \cdot \left(\mu_l \frac{\rho}{\rho_l} \nabla v \right) - \frac{\partial p}{\partial r} + B_r - \frac{\mu_l}{\kappa} \frac{\rho}{\rho_l} (v - v_s) - \frac{2}{r} \mu_l \frac{\partial}{\partial \theta} \left(\frac{\rho}{\rho_l} (u - f_s u_s) \right) - \frac{1}{r^2} \mu_l \frac{\rho}{\rho_l} (v - f_s v_s) + \rho \left(f_s \frac{v_s^2}{r} + f_l \frac{v_l^2}{r} \right) \tag{3}$$

$$\frac{\partial(\rho h)}{\partial t} + \nabla \cdot (\rho \mathbf{v} h) = \nabla \cdot \left(\frac{k}{c_s} \nabla h \right) + \nabla \cdot \left(\frac{k}{c_s} \nabla (h_s - h) \right) - \nabla \cdot (\rho (h_l - h)(\mathbf{v} - \mathbf{v}_s)) \tag{4}$$

$$\frac{\partial(\rho f^\alpha)}{\partial t} + \nabla \cdot (\rho \mathbf{v} f^\alpha) = \nabla \cdot (\rho D \nabla f^\alpha) + \nabla \cdot (\rho D \nabla (f_l^\alpha - f^\alpha)) - \nabla \cdot (\rho (f_l^\alpha - f^\alpha)(\mathbf{v} - \mathbf{v}_s)) \tag{5}$$

where the buoyancy forces per unit volume are defined as

$$B_\theta = -\rho g \sin\theta(\beta_T(T-T_o)+\beta_S(f_l^*-f_o^*)) \quad (6)$$

$$B_r = \rho g \cos\theta(\beta_T(T-T_o)+\beta_S(f_l^*-f_o^*)). \quad (7)$$

Mean mixture theory is used to define the continuum density, velocity, enthalpy, and species mass fraction appearing in equations (1)–(5)

$$\rho = g_s\rho_s+g_l\rho_l \quad (8)$$

$$\mathbf{v} = f_s\mathbf{v}_s+f_l\mathbf{v}_l \quad (9)$$

$$h = f_sh_s+f_lh_l \quad (10)$$

$$f^* = f_sf_s^*+f_lf_l^* \quad (11)$$

and continuum transport properties are similarly defined

$$k = g_sk_s+g_lk_l \quad (12)$$

$$D = f_lD_l^*. \quad (13)$$

Use of a volume averaged thermal conductivity in the mushy region is analogous to assuming a parallel thermal resistance in the solid and liquid phases. As there are no experimental data available for the effective thermal conductivity of aqueous Na_2CO_3 and because there is no evidence to indicate that other models yield more accurate estimates of k in the mushy region, the simple, volume averaged approach was deemed suitable. Moreover, the continuum thermal conductivity is consistent with the nature of conduction heat transfer in the mushy region since diffusion of heat occurs parallel to the direction of dendritic growth, which for the present case is primarily one-dimensional (radial). Thermal contact resistance between the isothermal, inner cylinder and the solid phase was assumed to be negligible.

Incorporation of Darcy's law into the continuum momentum equations to account for flow in the porous mushy region requires that an empirical correlation be introduced for the permeability, κ. In the metallurgical literature, a frequently used permeability model that has been verified experimentally using metal alloys with $g_l \leqslant 0.3$ is that κ is proportional to g_l^2 [11–13]. Using an organic compound that froze dendritically, Okamoto *et al.* [14] determined that the permeability (for $g_l > 0.3$) exhibited a stronger dependence on the liquid volume fraction than would be characterized by the g_l^2 model. Recognizing that the g_l^2 model was inappropriate for large liquid volume fractions, West [15] proposed a permeability model which combined the g_l^2 expression with a κ–g_l relationship based on flow through an array of spherical particles. This model is more consistent with the actual variation of κ in the mushy region since it insures that infinite permeability prevails when $g_l = 1$. However, the assumption that the permeability in the mushy region can be likened to flow through spherical particles is suspect. To the authors' knowledge, there are no experimental data for κ of the Na_2CO_3 solution used in this study, and thus, it is unclear if the existing permeability data/models are applicable for the present case. Hence, the Kozeny–Carman equation was selected because it possesses the desired limiting features as g_l varies from unity to zero and has been successfully implemented by other investigators [16]. The expression is of the form

$$\kappa = \kappa_o\left[\frac{g_l^3}{(1-g_l)^2}\right] \quad (14)$$

where κ_o is determined from the specific morphology of the system. For the present study, κ_o is taken to be 5×10^{-11} m^2, which is based on geometric data (dendrite arm spacing) for another aqueous salt solution [16]. Attempts were not made to account for a directional dependence of κ, although experimental data [14] suggest that permeability for flow parallel to the direction of primary dendrites is significantly greater than for normal flow.

The equilibrium phase diagram for aqueous Na_2CO_3, which has a eutectic temperature and composition (Na_2CO_3 mass fraction) of $T_e = -2.1$°C and $f_e^* = 0.059$, respectively, is shown in Fig. 2. As in past studies [8, 10], the phase diagram was utilized to obtain phase (f_l,f_s) and component (f_l^*,f_s^*) mass fractions, as well as temperature, from knowledge of the mixture composition (f^*) and enthalpy (h). However, unlike past studies, due to significant curvature of the liquidus line for hypereutectic compositions ($f^* > f_e^*$), the phase diagram was not linearized and a quadratic curve fit was used for the liquidus.

The continuum formulation is based upon several major assumptions: (i) laminar flow, (ii) Newtonian fluid, (iii) local thermodynamic equilibrium, (iv) constant properties, (v) constant density ($\rho_l = \rho_s$) except for variations in the buoyancy force, (vi) isotropic permeability, and (vii) negligible species diffusion in the solid phase. The condition of thermodynamic

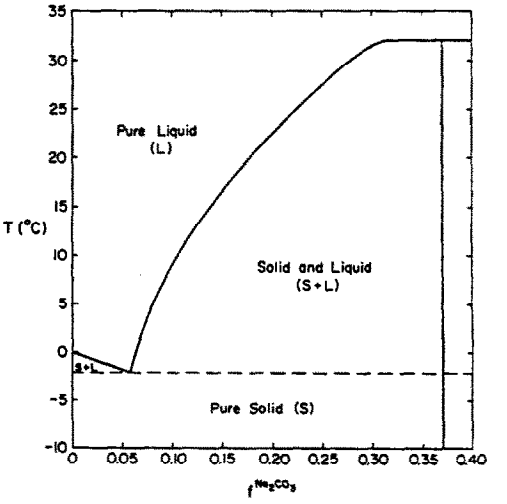

FIG. 2. Equilibrium phase diagram for Na_2CO_3–H_2O.

equilibrium permits the use of the equilibrium phase diagram, while the assumption of constant density implies a non-deforming solid and a saturated solid/liquid mixture.

The spatially-elliptic, temporally-parabolic equations (1)–(5) were solved using a control-volume based, upwind, finite-difference scheme [17], and details of the solution procedure are provided elsewhere [18]. In this study, however, the technique utilized to evaluate the temperature of control volumes in the mushy region was modified to account for the curvature of the liquidus line. The solid phase composition for hypereutectic compositions is a constant. A generalized equilibrium lever law was developed which related the solid (or liquid) mass fraction to the mean, solid, and liquid phase compositions. In turn, the liquid phase composition was expressed in terms of temperature using a quadratic curve fit for the liquidus line. With the average species mass fraction calculated from equation (5) and the mixture enthalpy known from equation (4), equation (10) could be expressed solely in terms of temperature. Hence, the quadratic equation for temperature, which arises when the liquidus line is assumed to be linear [13], was replaced by a cubic equation that was solved using an exact root-finding technique.

Prior to performing the proposed calculations, the continuum equations (1)–(5) were used to simulate natural convection (without solidification) in a horizontal annulus. Results from these calculations were in good agreement with the experimental results of Kuehn and Goldstein [19]. Discretization of the calculation domain for the phase change simulation was accomplished with the 40×40 biased grid shown in Fig. 1. The dimensions of the domain correspond to those of a test cell [20] for which data will be compared with the predictions of this study. Adiabatic boundary conditions were imposed for the outer cylinder and the vertical plane of symmetry, while an isothermal inner cylinder was maintained for $t > 0$. The simulation was initiated with a superheated aqueous Na_2CO_3 solution of uniform composition f_o^* and temperature T_o. For the present study, the solid phase translational velocities, u_s and v_s, were zero. The computations were performed using thermophysical property data (Table 1) obtained from various sources [21, 22]. For $t < 12$ min, a time step of 3 s was utilized, the accuracy of which was verified by using smaller time steps during test simulations of the initial transient. A time step of 6 s was used for $t > 12$ min.

Table 1. Thermophysical properties of Na_2CO_3–H_2O

	Solid	Liquid
Density (kg m^{-3})	1188	1188
Viscosity (kg m^{-1} s^{-1})	—	2.863×10^{-3}
Thermal expansion coefficient (K^{-1})	—	4.103×10^{-4}
Solutal expansion coefficient	—	0.884
Thermal conductivity (W m^{-1} K^{-1})	2.0	0.608
Specific heat (J kg^{-1} K^{-1})	1872	3615
Diffusivity (m^2 s^{-1})	—	7.0×10^{-10}
Latent heat (J kg^{-1})		3.232×10^5

Grid independent results were confirmed by simulating the first 3 min of solidification using a 50×50 grid and comparing the average heat extraction rate, $\bar{q}_c$, and the total solid formed, $\bar{f}_s$, with values obtained using the 40×40 grid (Fig. 3). Comparison of local values of temperature for the two grids (Fig. 4(a)) reveals excellent agreement for locations that remain above T_e during the first 3 min of solidification. Although locations that undergo complete solidification ($T < T_e$) appear to agree less favorably (Fig. 4(b)), the oscillations exhibited by both grids at a given location occur around a common mean value. The physically unrealistic plateaus noted in $\bar{q}_c$ and the temperatures in Fig. 4(b) may be attributed to the enthalpy-based formulation of the energy equation [18]. All computations were performed using a CYBER 205 supercomputer in which solution convergence, with the 40×40 grid, required 15–75 CPU s for each second of real time. Total CPU time for the simulation was approximately 15 h.

3. EXPERIMENTAL PROCEDURES

Christenson and Incropera [20] used an aqueous Na_2CO_3 solution to experimentally study solidification for the geometry of interest. Phase change was induced on an isothermal ($T_{s,i} = -20$°C), horizontal cylinder ($D_i = 25.4$ mm), while a well-insulated condition was maintained at the outer cylinder ($D_o = 101.6$ mm). Temperature distributions in the radial direction were recorded by four thermocouple rakes located at the axial midplane of the test cell and at circumferential locations (measured from the top of the cavity) of $\theta = 0$, 45, 135 and 180 deg (Table 2). A single fiber optic refractometer was used to monitor variations in liquid composition at a fixed location. By considering four initial compositions of Na_2CO_3 solution ($f_o^* = 0.02$, 0.07, 0.10, and 0.17), the effects of augmenting and non-augmenting thermal and solutal flows were examined.

Convection associated with freezing of the hypoeutectic composition ($f_o^* = 0.02$) was characterized by descending thermally induced boundary layer flow around the inner cylinder, which was augmented by a solutal downflow due to rejection of the denser constituent (Na_2CO_3) in the mushy region. In contrast, counter thermal and solutal flows were associated with the hypereutectic ($f_o^* > 0.059$) initial compositions, for which ascending solutal plumes were observed at the top of the cylinder. The opposing thermal and solutal flows exhibited behavior characteristic of double-diffusive fingering [23] and ultimately yielded a series of double-diffusive layers. With increasing initial composition, the strength of the solutal flow increased and the number of double-diffusive layers decreased. The solidification rate around the circumference of the inner cylinder varied

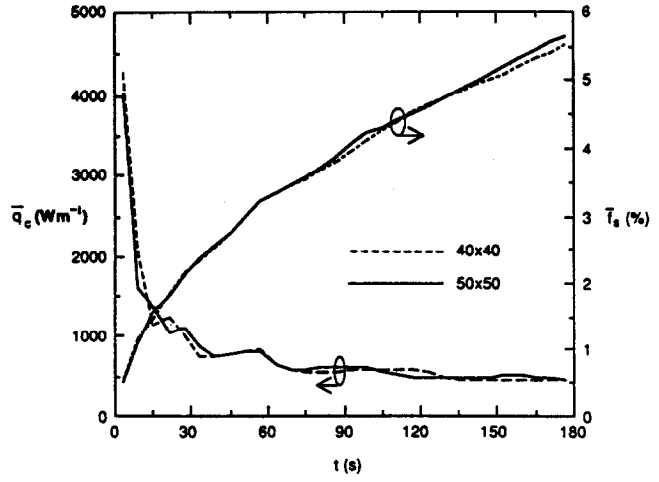

FIG. 3. Comparison of heat rate and solid mass fraction predictions for 40×40 and 50×50 grids.

according to local composition. Growth of solid phase was enhanced in regions where the bulk liquid remained at or near the original composition, while growth was inhibited in regions of nearly eutectic composition. For hypereutectic initial compositions, eccentric growth of the mushy region was marked by more pronounced dendritic formation along the bottom of the casting.

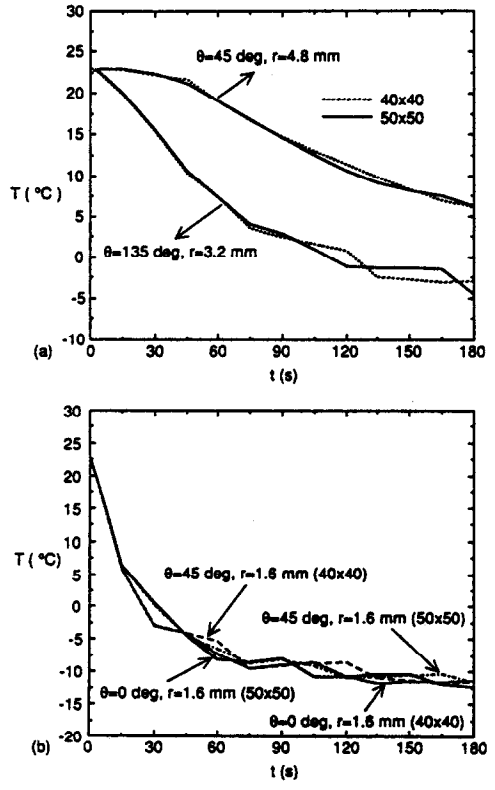

FIG. 4. Comparison of temperature histories for 40×40 and 50×50 grids: (a) $\theta = 45$ deg, $r = 4.8$ mm and $\theta = 135$ deg, $r = 3.2$ mm; (b) $\theta = 0$ deg, $r = 1.6$ mm and $\theta = 45$ deg, $r = 1.6$ mm.

Table 2. Radial position of thermocouples

Thermocouple	$(r - r_i)$ (mm)
1	0.0
2	1.6
3	4.8
4	8.0
5	11.1
6	15.9
7	25.4

4. NUMERICAL RESULTS

The most interesting behavior of solidification in an aqueous Na_2CO_3 solution occurs for hypereutectic compositions which are characterized by a rejection of water-rich liquid. Rejection of this less dense fluid, which is opposed by thermally induced convection, is manifested by the evolution of double-diffusive interfaces in the region around the chilled cylinder. Since the strength of the solutal upflow and the extent of mushy region formation increase with increasing Na_2CO_3 composition, the largest initial composition ($f_o^z = 0.17$) of the experimental study [20] was selected for a numerical simulation of opposing thermal and solutal effects.

Conditions at $t = 2$ min are illustrated in Figs. 5(a)–(d), which include the velocity field and streamlines, with the solidus and liquidus locations superimposed, contours of constant temperature, and lines of constant Na_2CO_3 composition in the liquid phase. To discern the relative strengths of the streamlines, the maximum streamfunction of the clockwise recirculation is designated as $|\psi_{max}|$ and is plotted in increments of $|\psi_{max}|/15$, while the maximum streamfunction of the counterclockwise recirculation is designated as ψ_{max} and is plotted in increments of $\psi_{max}/4$. Isotherms are plotted in terms of a dimensionless temperature, $T^* = (T - T_{s,i})/(T_{max} - T_{s,i})$, where T_{max} is the maximum temperature in the annu-

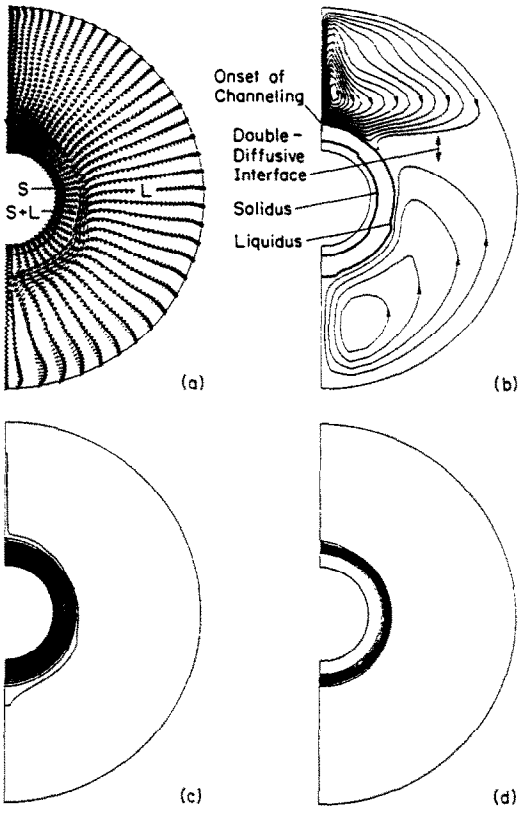

FIG. 5. Solidification behavior at $t = 2$ min for an aqueous Na_2CO_3 solution in a horizontal, cylindrical annulus ($f^{\alpha}_{o} = 0.17$, $T_o = 23°C$, $T_{s,i} = -20°C$): (a) velocity ($|v_{max}| = 6.4$ mm s^{-1}); (b) streamlines ($|\psi_{max}| = 1.01 \times 10^{-2}$ kg m^{-1} s^{-1}, $\psi_{max} = 2.49 \times 10^{-2}$ kg m^{-1} s^{-1}); (c) isotherms ($T_{max} = 22.9°C$); (d) isocompositions ($f^{\alpha}_{max} = 0.17$).

lus and decreases with increasing time. Lines of constant liquid composition are also represented nondimensionally by $f^{*}_{l} = (f^{\alpha}_{l} - f^{\alpha}_{l,e})/(f^{\alpha}_{l,max} - f^{\alpha}_{l,e})$, with species α corresponding to Na_2CO_3 and the solidus line representing the eutectic liquid composition $f^{*}_{l} = 0$. Due to the redistribution of species which accompanies solidification, $f^{\alpha}_{l,max}$ is a decreasing function of time.

For one side of the vertical plane of symmetry, Figs. 5(a) and (b) reveal several important features of the flow field. Rejection of lighter, water-rich solution occurs during phase change in the two-phase region because of a decrease in liquid phase Na_2CO_3 solubility with decreasing temperature. Hence, in the mushy region, a solutally driven upflow is established, which provides cold, water-rich fluid to the plume exiting at $\theta = 0$ deg. The plume is primarily sustained, however, by the release of Na_2CO_3 deficient fluid near the liquidus front and the top of the casting ($\theta \leqslant 40$ deg). This plume is responsible for formation of a clockwise recirculation in the upper region of the cavity. Velocities within the recirculating cell are typically 1.5 to 2 orders of magnitude greater than those in the mushy region. Opposing the solutally driven plume/clockwise recirculation, there is a stronger thermally driven recirculation, which exists in the bottom two-thirds of the cavity and is a manifestation of the larger temperature difference between the liquidus front and the initial superheat of the bulk liquid.

Although the induced fluid motion suggests that convection should strongly influence growth of the solid and mushy regions, the isotherms and isocomps of Figs. 5(c) and (d) indicate that diffusion is the dominant transport mechanism during the early stages of phase change. The isotherms remain essentially concentric except for the subcooling associated with the ascending solutal and descending thermal plumes above and below the cylinder, respectively. Variations of the liquid concentration are largely confined to the mushy region, while the bulk liquid remains essentially at the initial composition. Accumulation of water-rich solution along the top centerline of the casting produces a localized freezing point depression relative to neighboring locations in the mush. This effect yields a small channel or segregate [1] of pure liquid which resists freezing (Fig. 5(b)). The small changes in temperature and concentration within the bulk fluid do not preclude development of the double-diffusive interface located at $\theta = 45$ deg. Contours of constant density (not shown) reveal that the bulk liquid, excluding the plumes, possesses net hydrodynamic stability, despite the unstable thermal condition resulting from the rejection of cool (water-rich) solution from the solutally driven plume.

As solidification proceeds ($t = 5$ min), the strength of the thermally induced downflow diminishes. Figs. 6(a) and (b), causing the horizontal, double-diffusive interface separating the counter-rotating cells to descend to $\theta \approx 110$ deg. Outflow of cold, water-rich fluid from the mushy region continues to be pronounced at $\theta = 0$ deg and is now accompanied by a much weaker outflow at $\theta \approx 45$ deg. The outflow at 45 deg promotes the formation of two clockwise-rotating cells above the interface. The channel of pure liquid continues to exist along the top centerline within the mush, but occupies a very narrow region ($0 \leqslant \theta \leqslant 2$ deg) extending radially inward from the liquidus to approximately 60% of the mushy region thickness. The pooling of cool, water-rich solution in the upper portion of the annulus is revealed by the isotherm and liquid isoconcentration lines of Figs. 6(c) and (d), respectively.

Erosion of the double-diffusive interface begins at approximately $t = 10$ min and is characterized by intrusion of the solutally-driven flow to $\theta = 180$ deg (Figs. 7(a) and (b)). This flow crosses the interface along the liquidus and enters the mushy region near the bottom of the cavity. Having penetrated the liquidus, fluid ascends within the mushy region (following the liquidus contour) to feed the plume exiting at the top of the cylinder. However, not all of the mushy region upflow near the liquidus rises to the top of the cylinder, as some fluid exits the mush in the region from approximately 40 to 90 deg. The temperature and liquid concentration contours, Figs. 7(c) and (d),

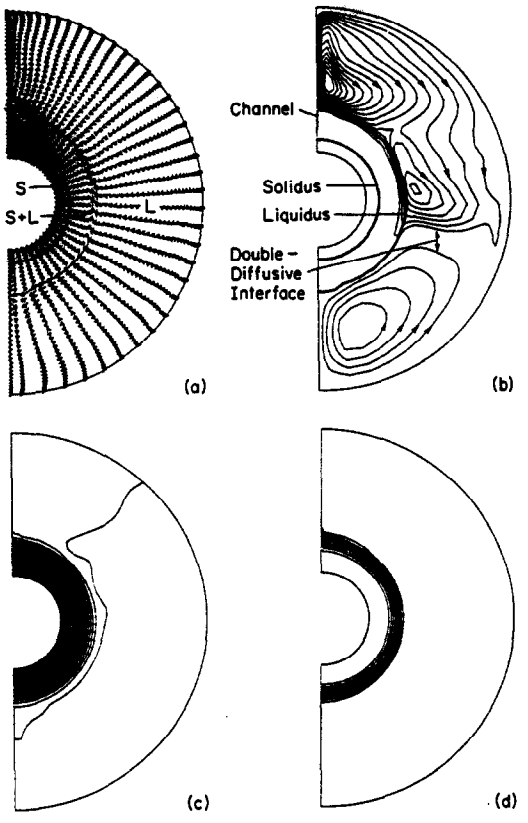

FIG. 6. Solidification behavior at $t = 5$ min for an aqueous Na_2CO_3 solution in a horizontal, cylindrical annulus ($f_o^z = 0.17$, $T_o = 23°C$, $T_{s,i} = -20°C$): (a) velocity ($|v_{max}| = 6.3$ mm s^{-1}); (b) streamlines ($|\psi_{max}| = 9.06 \times 10^{-3}$ kg m^{-1} s^{-1}, $\psi_{max} = 1.29 \times 10^{-2}$ kg m^{-1} s^{-1}); (c) isotherms ($T_{max} = 22.3°C$); (d) isocompositions ($f^z_{max} = 0.17$).

reveal unstable thermal and stable solutal stratification in the top half of the bulk fluid. However, overall stability is maintained because the destabilizing thermal field is more than offset by the stabilizing solutal field, as verified by contours of constant density (not shown).

With increasing time, the clockwise recirculation of Na_2CO_3 deficient fluid penetrates further to the bottom of the annulus. A remnant of the double-diffusive interface persists at $t = 17$ min, Figs. 8(a) and (b), but the strength of the thermally driven flow is approximately an order of magnitude smaller than that of the solutal flow. As at previous times, advection in the mushy region is primarily in the circumferential direction, with localized outflows occurring in the region $30 \leqslant \theta \leqslant 150$ deg. The primary outflow at $\theta = 0$ deg continues to enhance the accumulation of water-rich liquid along the top centerline of the casting, thereby sustaining the channeling effect noted at previous times. This effect is further delineated in Figs. 8(c) and (d), which reveal the accumulation of cooler, less-concentrated solution near the centerline.

The time span from $t = 17$ to 25 min marks the development of another channel in the top region of the mush. Localized remelting produces a pocket of water-rich liquid which is aligned with the flow direction in the mushy region, Figs. 9(a) and (b). However, aside from the presence of the two segregates in the upper region of the mush, the interdendritic flow does not appreciably alter the concentricity of solid growth. The solidus and liquidus fronts are nearly concentric at $t = 25$ min, despite the unstable thermal and stable solutal stratification that occurs in the bulk liquid, Figs. 9(c) and (d).

Due to inherently large CPU time requirements, the simulation was terminated at $t = 30$ min. The most noteworthy feature of phase change at this time, Fig. 10, is the occurrence of enhanced mushy region formation at the bottom of the cavity, causing a slightly eccentric liquidus front. Solidus formation is inhibited in the top region of the cavity due to water enrichment of the bulk fluid and the associated liquidus temperature depression.

5. COMPARISON OF PREDICTED AND EXPERIMENTAL RESULTS

At times roughly corresponding to those of Figs. 5–10, hydrodynamic conditions and the position of

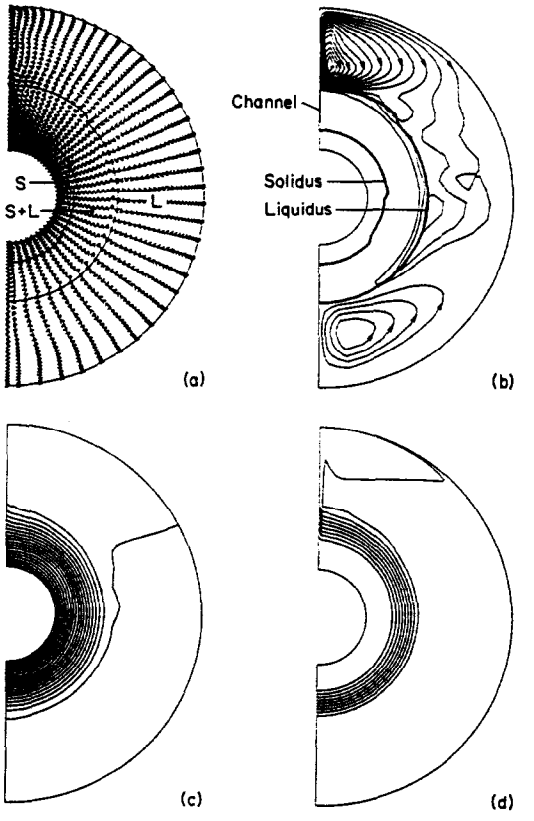

FIG. 7. Solidification behavior at $t = 10$ min for an aqueous Na_2CO_3 solution in a horizontal, cylindrical annulus ($f_o^z = 0.17$, $T_o = 23°C$, $T_{s,i} = -20°C$): (a) velocity ($|v_{max}| = 6.3$ mm s^{-1}); (b) streamlines ($|\psi_{max}| = 7.94 \times 10^{-3}$ kg m^{-1} s^{-1}, $\psi_{max} = 5.84 \times 10^{-3}$ kg m^{-1} s^{-1}); (c) isotherms ($T_{max} = 21.0°C$); (d) isocompositions ($f^z_{max} = 0.17$).

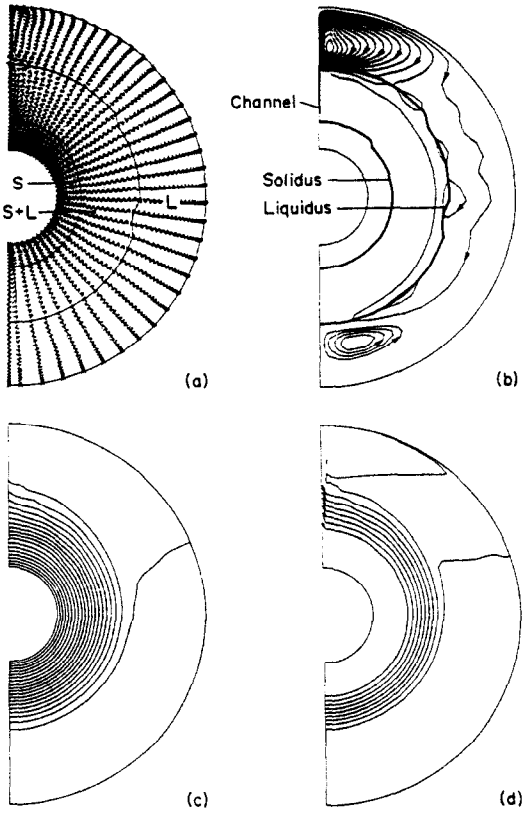

FIG. 8. Solidification behavior at $t = 17$ min for an aqueous Na_2CO_3 solution in a horizontal, cylindrical annulus ($f^2_o = 0.17$, $T_o = 23°C$, $T_{s,i} = -20°C$): (a) velocity ($|v_{max}| = 5.4$ mm s^{-1}); (b) streamlines ($|\psi_{max}| = 6.67 \times 10^{-3}$ kg m^{-1} s^{-1}, $\psi_{max} = 7.40 \times 10^{-4}$ kg m^{-1} s^{-1}); (c) isotherms ($T_{max} = 20.0°C$); (d) isocompositions ($f^2_{max} = 0.17$).

the solidus and liquidus fronts were photographed using the shadowgraph technique, as well as front illumination of the test cell. The shadowgraphs of Figs. 11(a)–(f) reveal features of the flow, while photographs obtained with front illumination, Figs. 12(a)–(f), better delineate the solid, mushy and liquid regions.

The sequence of shadowgraphs discloses several significant features of the solidification process. From the onset of phase change, solutal upflow from the mushy region occurs in a broad zone the width of which approaches the diameter of the liquidus front. A more detailed investigation of conditions within the upflow, which was performed using dye injection [20], revealed the existence of a large number of small, randomly generated plumes of rejected water-rich solution. Double-diffusive layering in the bulk liquid is also observed, with conditions proceeding from the creation, Fig. 11(c), downward propagation, Fig. 11(d), and eventual erosion, Fig. 11(e), of a single, horizontal, double-diffusive interface. The presence of additional, weaker interfaces above the major interface is seen in Figs. 11(c) and (d). Although not readily apparent in the shadowgraphs, the strength of the thermally-driven flow diminishes with increasing time. Additionally, slightly eccentric liquidus front growth is observed, Fig. 12, and occurs because a more favorable growth environment exists in the bottom of the cavity. That is, water enrichment in the top of the annulus depresses the liquidus temperature and retards solid formation. Note that solid and mushy regions are manifested by the light and dark rings, respectively, around the inner cylinder.

Comparisons between predicted and experimental results yielded mixed success. A major difference between the two results concerns the horizontal extent of the solutally-driven upflow, which is greatly underpredicted by the model. While the model predicts a thin, laminar plume driven by mushy region upflow, the shadowgraphs (Fig. 11) reveal a broad, turbulent plume which originates from local instabilities occurring over much of the top portion of the liquidus interface. The model predictions suggest a strong influence of water-rich fluid, which is rejected near the liquidus front with a significant circumferential velocity component. Such fluid feeds a solutal boundary layer adjoining the liquidus and ascends as a narrow plume centered at $\theta = 0$ deg. In contrast, the shadowgraphs suggest a strong upflow within the mushy region and hence the development of a highly

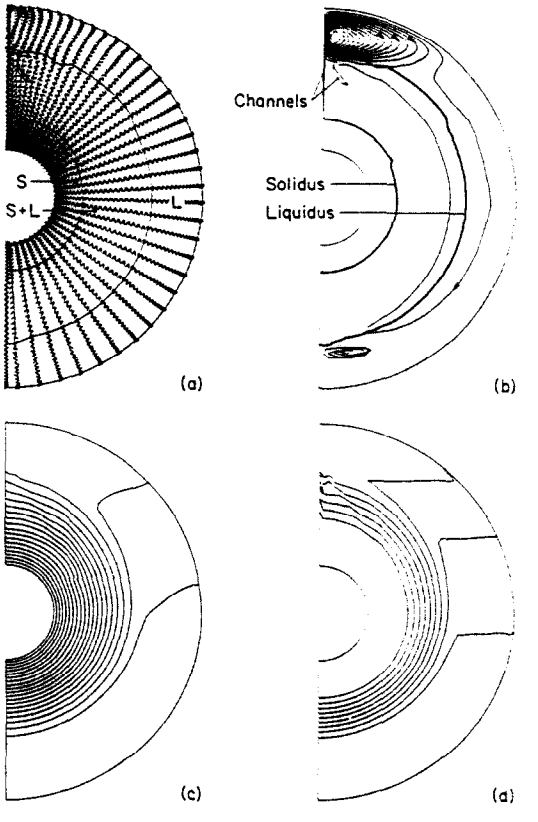

FIG. 9. Solidification behavior at $t = 25$ min for an aqueous Na_2CO_3 solution in a horizontal, cylindrical annulus ($f^2_o = 0.17$, $T_o = 23°C$, $T_{s,i} = -20°C$): (a) velocity ($|v_{max}| = 4.3$ mm s^{-1}); (b) streamlines ($|\psi_{max}| = 5.45 \times 10^{-3}$ kg m^{-1} s^{-1}, $\psi_{max} = 4.40 \times 10^{-5}$ kg m^{-1} s^{-1}); (c) isotherms ($T_{max} = 19.3°C$); (d) isocompositions ($f^2_{max} = 0.17$).

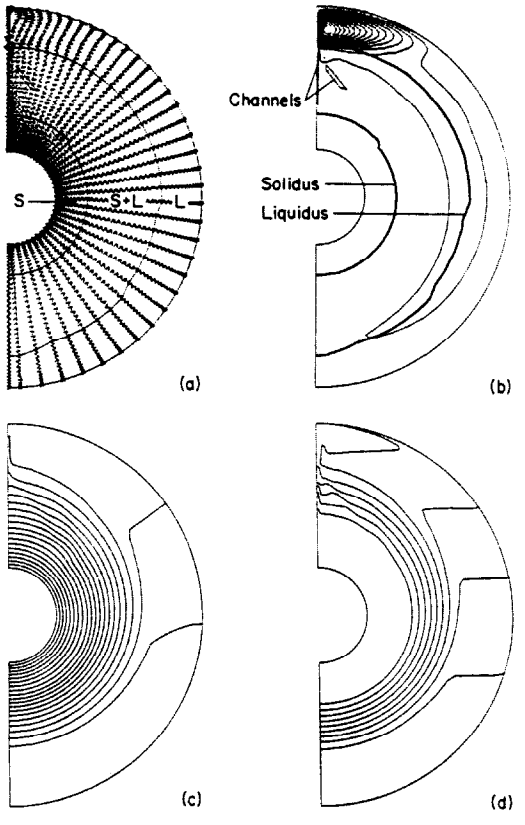

FIG. 10. Solidification behavior at $t = 30$ min for an aqueous Na_2CO_3 solution in a horizontal, cylindrical annulus ($f^x_o = 0.17$, $T_o = 23°C$, $T_{s,i} = -20°C$): (a) velocity ($|v_{max}| = 3.7$ mm s^{-1}); (b) streamlines ($|\psi_{max}| = 4.51 \times 10^{-3}$ kg m^{-1} s^{-1}, $\psi_{max} = 2.61 \times 10^{-6}$ kg m^{-1} s^{-1}); (c) isotherms ($T_{max} = 19.0°C$); (d) isocompositions ($f^x_{max} = 0.17$).

anisotropic permeability which is biased in the vertical direction. Directional characteristics of the mushy region permeability, as well as the manner in which they may vary with time, are unknown. Even with full knowledge of mushy region conditions, however, it is doubtful that prediction of the fine features of the transient, three-dimensional flow would be computationally feasible.

Evolution of the double-diffusive interface, including decay of the underlying, thermally-driven flow, is predicted well, although time scales for computed and observed interface locations and erosion differ. For instance, the model predicts interface erosion to begin at $t = 10$ min, when the interface is located at $\theta \approx 110$ deg, Fig. 7(b). In contrast, observations at this time, Fig. 11(c), reveal no erosion of the interface, which is positioned at $\theta \approx 80$ deg. Nevertheless, during the latter stages of the simulation, when no interface is predicted, Figs. 9(a) and (b), experimental conditions, Fig. 11(e), disclose only a very weak interface. Solution dependent remeshing of the computational domain to resolve large gradients, instead of using a fixed grid, would probably improve the model's ability to track the transient progression of the double-diffusive interface. However, an adaptive grid technique would considerably increase model complexity and simulation cost, which is already quite significant.

A general trend noted for all predicted physical phenomena (e.g. evolution of the double-diffusive interface) is that their onset and completion occur earlier than the corresponding observed events. Such behavior may be characteristic of the model's upwind finite-difference approach, which introduces artificial diffusion but yields physically realistic trends. An artificial enhancement of diffusion might expedite the decay of field variable gradients in the system, thereby resulting in more rapid transients relative to those observed. However, in view of uncertainties in model assumptions such as phase equilibrium, laminar flow and the nature of mushy region conditions, a definitive explanation of the foregoing differences cannot be provided at this time.

Growth of the pure solid phase, Figs. 12(a)–(f), appears to be unaffected by the interdendritic flow of colder, water-rich solution which forms during phase change. Concentric freezing of the solid implies that conduction is the primary mechanism for heat transfer at the solidus front. Numerical predictions for the solid thickness as a function of angular position track the experimental values reasonably well, with the data being, generally, slightly underestimated (Fig. 13). However, a comparison of numerical and experimental results for the mushy region thickness as a function of angular location (Fig. 14) reveals significant differences. The discrepancy is greatest for $\theta < 135$ deg and may be attributed to the model's inability to resolve the true nature of the solutally driven plume, to uncertainties in the material property data base (in particular, the permeability coefficient), and/or to other model assumptions such as validity of the Kozeny–Carman equation. In addition, the observations did not reveal the development of pockets of pure liquid in the mushy region near $\theta = 0$ deg. Prediction of the pockets is related to the thin solutally-driven plume which is fed, in part, by mushy region advection at $\theta = 0$ deg. Hence, an accumulation of water-rich solution, which resists freezing is predicted to occur along the centerline. However, as previously noted, the actual plume is not confined to the centerline, but is distributed across the liquidus front.

In Figs. 15(a) and (b), predicted temperatures are compared with measurements from two of the four thermocouple rakes. The temperature history of the chilled cylinder is also included and clearly illustrates that, over the course of the simulation, the cylinder is not isothermal as modelled. At radial locations above the cylinder ($\theta = 0$ deg, Fig. 15(a)), predicted and measured temperatures are in good agreement within the solid phase ($T < T_e$) but differ more significantly in the mushy and bulk liquid regions. Moreover, the model predicts lower temperatures at all but the outermost radial locations. These trends characterize other rake locations and are exhibited by the results for $\theta = 135$ deg, Fig. 15(b). Discrepancies between

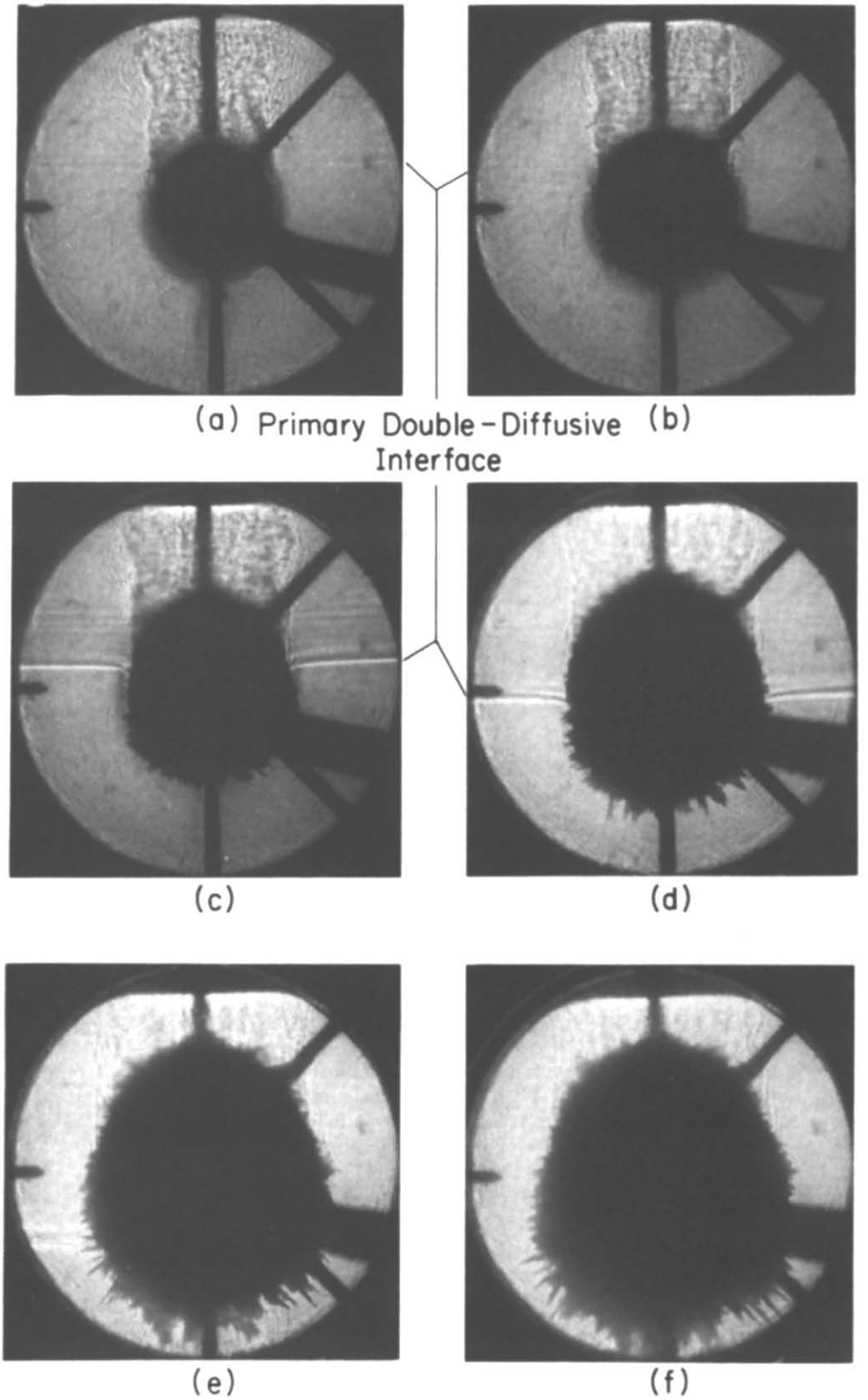

FIG. 11. Shadowgraphs of solidification for an aqueous Na_2CO_3 solution in a horizontal, cylindrical annulus ($f_0^2 = 0.17$, $T_0 = 23$ C, $T_{cs} = -20$ C): (a) $t = 2$ min; (b) $t = 5$ min; (c) $t = 10$ min; (d) $t = 16.5$ min; (e) $t = 25$ min; (f) $t = 30$ min.

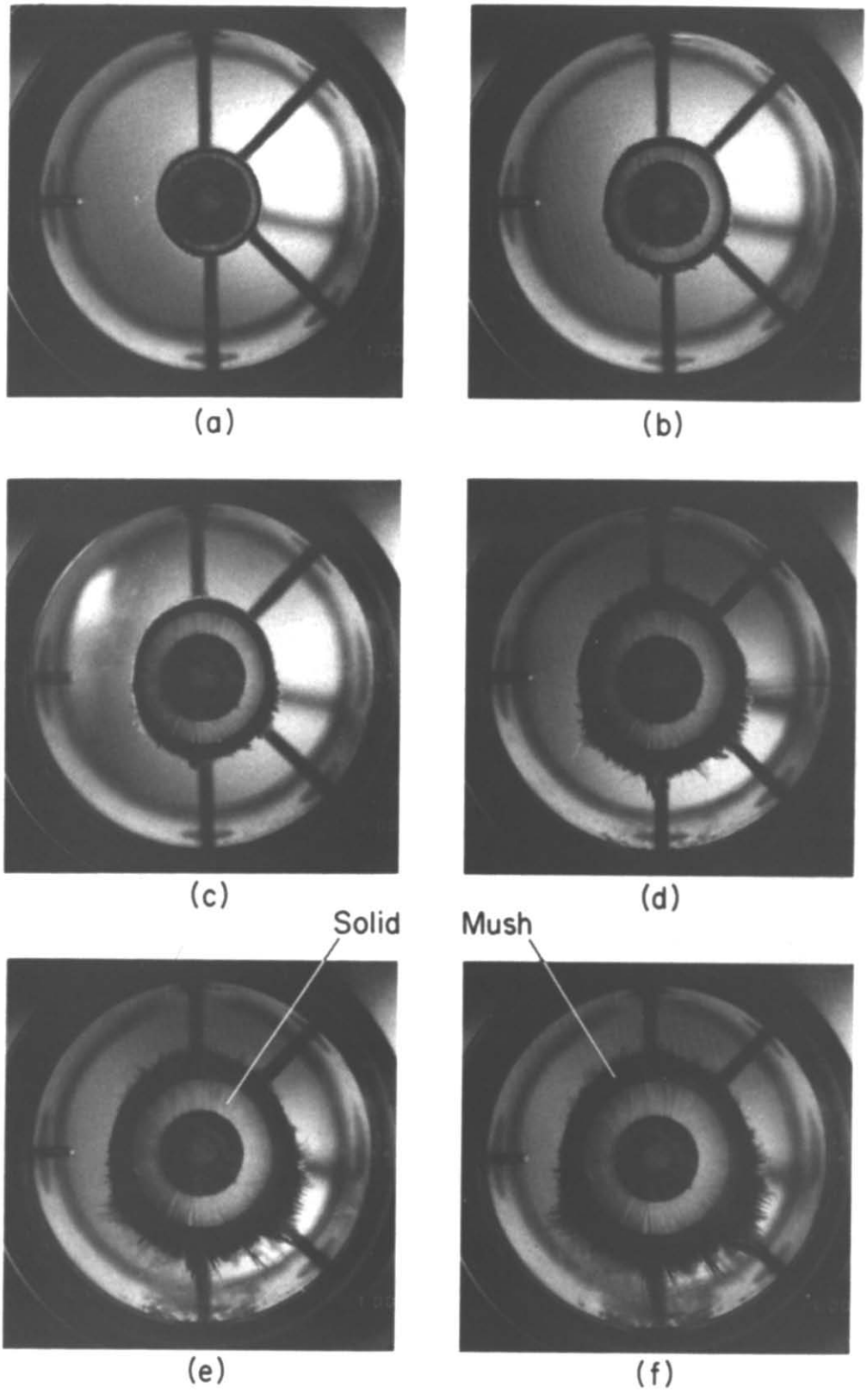

FIG. 12. Solidus and liquidus fronts during solidification of an aqueous Na_2CO_3 solution in a horizontal, cylindrical annulus ($f_0^s = 0.17$, $T_0 = 23^\circ C$, $T_{wi} = -20^\circ C$): (a) $t = 1.75$ min; (b) $t = 5.5$ min; (c) $t = 10.25$ min; (d) $t = 17$ min; (e) $t = 25.5$ min; (f) $t = 30.5$ min.

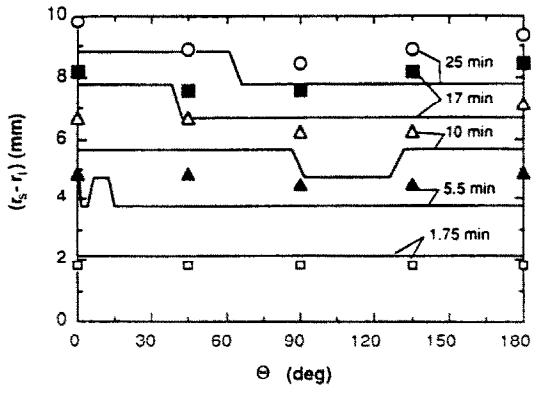

FIG. 13. Comparison of predicted (curves) and experimental (symbols) results for solid thickness $(r_s - r_i)$ as a function of θ for solidification of an aqueous Na_2CO_3 solution in a horizontal, cylindrical annulus ($f_0^s = 0.17$, $T_0 = 23°C$, $T_{s,i} = -20°C$).

measured and predicted temperatures are greatest at $\theta = 0$, 45 and 135 deg and are, at least in part, due to difficulties associated with resolving plume structure and its resulting effect on the clockwise recirculation of the cooler, water-rich solution, which is the dominant flow for $t > 10$ min.

Measured output from the concentration refractometer probe is compared with computed results in Fig. 16. The experimental data exhibit an unrealistic increase in Na_2CO_3 composition for $0 < t < 10$ min, which may be a result of slight calibration error or the probe's sensitivity to laboratory vibrations. Nevertheless, qualitative agreement is obtained, as the predicted values track the gradual decrease in solute composition of the bulk liquid at $r = 40$ mm and $\theta = 270$ deg. Mixing due the coalescence of the two recirculating layers separated by the diffusive interface does not appear to have caused appreciable changes in the solute concentration at this location.

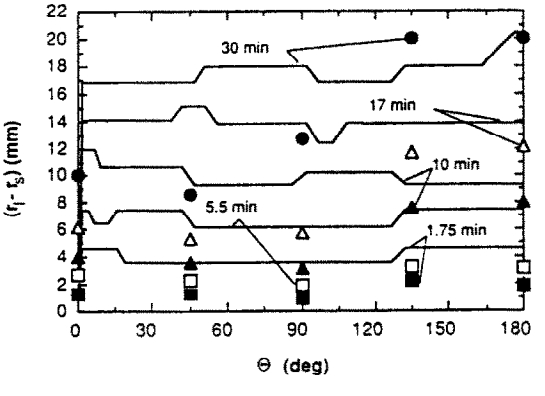

FIG. 14. Comparison of predicted (curves) and experimental (symbols) results for mush thickness $(r_l - r_s)$ as a function of θ for solidification of an aqueous Na_2CO_3 solution in a horizontal, cylindrical annulus ($f_0^s = 0.17$, $T_0 = 23°C$, $T_{s,i} = -20°C$).

6. SUMMARY

Solidification of an aqueous salt solution in a horizontal cylindrical cavity has been numerically simulated using a continuum formulation for the conservation equations. In particular, for a binary Na_2CO_3–H_2O solution, which rejected a less dense, water-rich liquid upon phase change and was characterized by extensive mushy region growth, the effect of opposing thermal and solutal convection was examined. Predicted and experimental results were compared to assess the capabilities and limitations of the model.

Solutal plume upflow due to the rejection of water-rich fluid was predicted, but the plume thickness was significantly smaller than that observed experimentally. A different mushy region permeability model and inclusion of a turbulence model which treats coherent structures may well be necessary to predict observed plume characteristics. Creation, downward movement and eventual erosion of a single double-diffusive interface was successfully predicted, although the simulated time scales were less than those observed experimentally. The strength of thermally-driven convection beneath the predicted double-diffusive interface decayed with increasing time, which was in qualitative agreement with observations. Improvements may be realized by using a power law formulation [17] in the finite-difference approximation and a grid remeshing algorithm which clusters control volumes in regions of large gradients and minimizes resolution in areas where spatial variations of the field variables are small. The latter alteration represents a significant increase in model sophistication and computational cost.

Flow visualization clearly showed the existence of turbulence along the top portion of the cylindrical casting. The predicted mixing processes in the liquid of this region would presumably be slower than actuality when a turbulence model is not utilized to augment molecular diffusion. Predicted results, however, indicated that the overall solidification process occurred more rapidly than the actual phase change. Hence, assuming that the lack of a turbulence model represents the only physical shortcoming of the simulation, the inclusion of turbulence would only serve to further expedite the predicted solidification process. Improvement to predictions would most likely require that other parameters, such as the permeability model, be known with greater certainty before accounting for the effects of turbulence.

Comparison of model predictions and experimental data for development of the solid and mushy regions revealed that the model slightly underpredicted solid growth and significantly overpredicted mushy region growth. Due possibly to deviation of the simulated plume shape from the observed shape, predicted mushy region channel formation was not noted experimentally. Previous predictions using the continuum model and another salt solution (NH_4Cl–H_2O) more

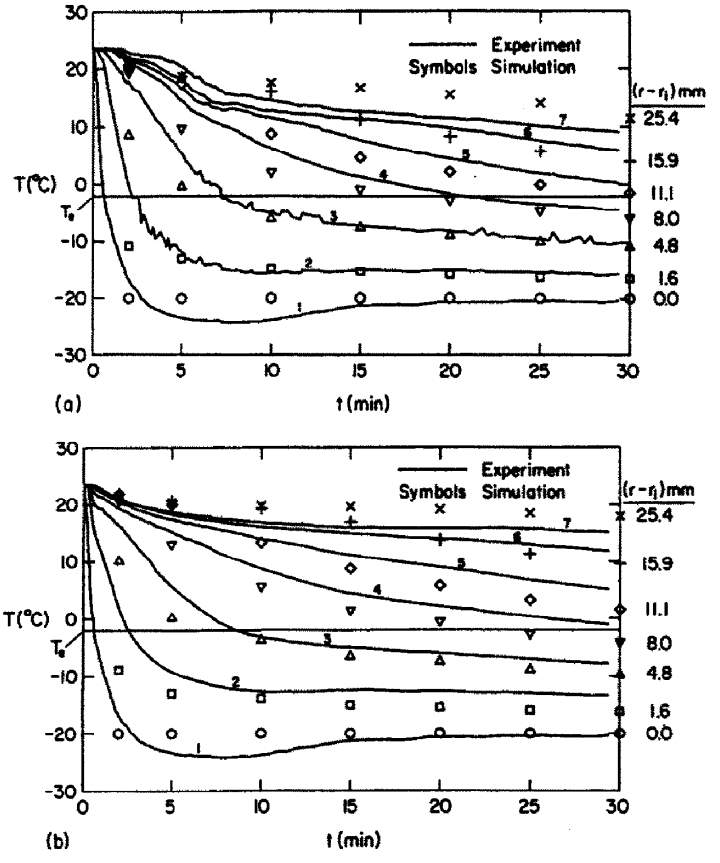

FIG. 15. Comparison of predicted and measured radial temperature distributions as a function of time for solidification of an aqueous Na_2CO_3 solution in a horizontal, cylindrical annulus ($f_o^* = 0.17$, $T_o = 23°C$, $T_{s,i} = -20°C$): (a) $\theta = 0$ deg; (b) $\theta = 135$ deg.

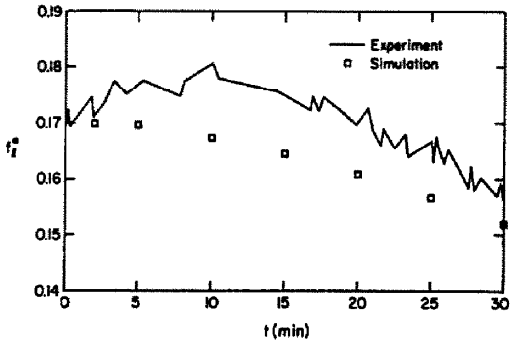

FIG. 16. Comparison of predicted and measured Na_2CO_3 composition at ($r = 40$ mm, $\theta = 270$ deg) as a function of time for solidification of an aqueous Na_2CO_3 solution in a horizontal, cylindrical annulus ($f_o^* = 0.17$, $T_o = 23°C$, $T_{s,i} = -20°C$).

severely underestimated growth of the solid phase [9]. Improved agreement in the present study may be the result of a more reliable property data base and/or use of the actual liquidus line curvature, rather than assumed linearity. However, the improvement may be fortuitous since considerable uncertainties exist with respect to the turbulent nature of the solutally-driven plume and modelling of the porous mushy region.

Predictions and measured temperatures for the solid region were in good agreement. Slightly less favorable agreement was obtained for the mushy and liquid regions, with lower temperatures predicted for all locations except the outermost position. The observed gradual decrease in liquid concentration at a fixed location in the bulk liquid was corroborated by the simulation.

Acknowledgements—One of the authors (D.G.N.) is grateful for support provided by the National Aeronautics and Space Administration under the Graduate Student Researchers Program. Support of this work has been provided by the U.S. Department of Energy under Award Number DEFG02-87ER13759.

REFERENCES

1. K. M. Fisher, The effects of fluid flow on the solidification of industrial castings and ingots, *PhysicoChem. Hydrodyn.* 2, 311–326 (1981).
2. G. A. Lane, *Solar Heat Storage: Latent Heat Material*, Vol. I. CRC Press, Boca Raton, Florida (1983).
3. S. Ostrach, Fluid mechanics in crystal growth—The 1982 Freeman Scholar Lecture, *J. Fluids Engng* 105, 5–20 (1983).
4. Ch. Korber and M. W. Scheiwe, Observations on the nonplanar freezing of aqueous salt solutions, *J. Crystal Growth* 61, 307–316 (1983).

5. M. E. Thompson and J. Szekely, Mathematical and physical modelling of double-diffusive convection of aqueous solutions crystallizing at a vertical wall, *J. Fluid Mech.* **187**, 409–433 (1988).
6. W. D. Bennon and F. P. Incropera, A continuum model for momentum, heat and species transport in binary solid–liquid phase change systems—I. Model formulation, *Int. J. Heat Mass Transfer* **30**, 2161–2170 (1987).
7. N. Shamsundar and E. M. Sparrow, Analysis of multidimensional conduction phase change via the enthalpy method, *J. Heat Transfer* **97**, 333–340 (1975).
8. W. D. Bennon and F. P. Incropera, A continuum model for momentum, heat and species transport in binary solid–liquid phase change systems—II. Application to solidification in a rectangular cavity, *Int. J. Heat Mass Transfer* **30**, 2171–2187 (1987).
9. M. S. Christenson, W. D. Bennon and F. P. Incropera, Solidification of an aqueous ammonium chloride solution in a rectangular cavity—II. Comparison of predicted and measured results. *Int. J. Heat Mass Transfer* **32**, 69–79 (1989).
10. C. Beckermann and R. Viskanta, Double-diffusive convection during dendritic solidification of a binary mixture, *PhysicoChem. Hydrodyn.* **10**, 195–213 (1988).
11. R. Nasser-Rafi, R. Deshmukh and D. R. Poirier, Flow of interdendritic liquid and permeability in Pb-20 wt pct Sn alloys, *Metall. Trans. A* **16A**, 2263–2271 (1985).
12. N. Streat and F. Weinberg, Interdendritic fluid flow in a lead–tin alloy, *Metall. Trans. B* **7B**, 417–423 (1976).
13. T. S. Piwonka and M. C. Flemings, Pore formation in solidification, *Trans. TMS–AIME* **236**, 1157–1165 (1966).
14. T. Okamoto, K. Murakami and A. Shiraishi, U.S.–Japan Cooperative Science Program Seminar on Solidification Processing, NSF (U.S.A.) and JSPS, Dedham, Massachusetts, pp. 97–112 (1983).
15. R. West, On the permeability of the two-phase zone during solidification of alloys, *Metall. Trans. A* **16A**, 693 (1985).
16. S. Asai and I. Muchi, Theoretical analysis and model experiments on the formation mechanism of channel-type segregation, *Trans. ISIJ* **18**, 90–98 (1978).
17. S. V. Patankar, *Numerical Heat Transfer and Fluid Flow*. Hemisphere, Washington, DC (1980).
18. W. D. Bennon and F. P. Incropera, Numerical analysis of binary solid–liquid phase change using a continuum model, *Numer. Heat Transfer* **13**, 277–296 (1988).
19. T. H. Kuehn and R. J. Goldstein, An experimental and theoretical study of natural convection in the annulus between horizontal concentric cylinders, *J. Fluid Mech.* **74**, 695–719 (1976).
20. M. S. Christenson and F. P. Incropera, Experiments on solidification of an aqueous sodium carbonate solution in a horizontal cylindrical cavity, *J. Heat Transfer* **111**, 998–1005 (1989).
21. *International Critical Tables and Numerical Data, Physics, Chemistry and Technology*, Vols 1–5 (1928).
22. *Thermophysical Properties Research Literature Retrieval Guide*, Vols 1 and 6. IFI/Plenum, New York (1982).
23. J. S. Turner, *Buoyancy Effects in Fluids*. Cambridge University Press, London (1979).

SIMULATION NUMERIQUE DE LA SOLIDIFICATION D'UN ANNEAU CYLINDRIQUE, HORIZONTAL, REMPLI D'UNE SOLUTION SALEE AQUEUSE

Résumé—Une étude numérique de la solidification d'une solution binaire de Na_2CO_3 dans un espace annulaire cylindrique est faite en utilisant une formulation de continuum basée sur un schéma de différences finies avec volume de contrôle. Les conditions initiales sont sélectionnées pour faciliter l'etude de la convection thermique et solutale, accompagnée de la croissance de la zone spongieuse. Les résultats numériques sont comparés aux données expérimentales avec un succès très relatif. Un accord est obtenu pour le mécanisme global de solidification et les phénomènes physiques associés. Néanmoins l'épaisseur du panache ascendant par convection solutale est sensiblement plus petite que celle observée. L'evolution des couches doublement diffusives est prédite mais pour un temps plus court que celui observée expérimentalement. Un bon accord est obtenu entre calcul et expérience pour la croissance du solide, mais l'épaisseur de la région spongieuse est nettement surestimée.

NUMERISCHE UNTERSUCHUNG DER VERFESTIGUNGSVORGÄNGE IN EINER WÄSSRIGEN SALZLÖSUNG IN EINEM WAAGERECHTEN ZYLINDRISCHEN RINGRAUM

Zusammenfassung—Eine rechnerunterstützte Untersuchung der Erstarrung einer binären Na_2CO_3-Lösung in einem horizontalen zylindrischen Ringraum wurde unter Verwendung eines Finite-Volumina-Verfahrens durchgeführt. Die Anfangsbedingungen sind so gewählt, daß die Untersuchung der gegenläufigen thermischen und konzentrationsgetriebenen Konvektion mit ausgeprägtem Wachstum eines Mischgebietes erleichtert wird. Numerische Ergebnisse werden mit experimentellen Daten verglichen—mit unterschiedlichem Erfolg. Es wird qualitative Übereinstimmung für den Erstarrungsprozeß als ganzen und die damit zusammenhängenden physikalischen Phänomene erreicht. Jedoch ist die Dicke der Strömungsfahnen, die für die konzentrationsgetriebene Aufwärtsströmung berechnet wird, erheblich kleiner als der beobachtete Wert. Die Entwicklung von doppelt-diffusiven Schichten wird zwar vorhergesagt, jedoch weit geringer als dies im Experiment zu beobachten ist. Gute Übereinstimmung besteht zwischen berechneten und gemessenen Ergebnissen für das Wachstum der festen Phase, doch wird die Dicke des Mischgebiets wesentlich zu groß berechnet.

ЧИСЛЕННОЕ МОДЕЛИРОВАНИЕ ПРОЦЕССА ЗАТВЕРДЕВАНИЯ В ГОРИЗОНТАЛЬНОМ ЦИЛИНДРИЧЕСКОМ КОЛЬЦЕВОМ КАНАЛЕ, ЗАПОЛНЕННОМ ВОДОСОЛЕВЫМ РАСТВОРОМ

Аннотация—С помощью метода конечных разностей численно исследуется процесс затвердевания бинарного раствора Na_2CO_3 в горизонтальном цилиндрическом кольцевом канале. Начальные условия выбирались таким образом, чтобы облегчить изучение противодействующих явлений: тепловой конвекции и конвекции при растворении вещества, сопровождаемых интенсивным ростом двухфазной зоны. Совпадение численных и экспериментальных данных удовлетворительно не во всех случаях. В общем получено качественное соответствие для процесса затвердевания и связанных с ним физических явлений. Рассчитанный временный масштаб эволюции диффузионных слоев оказался гораздо меньшим, чем в экспериментах. Получено хорошее соответствие между рассчитанными и измеренными данными для роста твердой фазы, в то время как значение толщины двухфазной зоны оказалось значительно завышенным.